RSC Advances

ROYAL SOCIETY OF CHEMISTRY

PAPER

View Article Online
View Journal | View Issue

Check for updates

Cite this: *RSC Adv.*, 2023, **13**, 27634

High-performance microwave absorption by optimizing hydrothermal synthesis of $BaFe_{12}O_{19}@MnO_2$ core–shell composites

Erlina Yustanti, *[ab] Alfian Noviyanto, [cd] Muhammad Ikramullah,[a] Yogie Anes Marsillam,[a] Yana Taryana[e] and Ahmad Taufiq[f]

Received 28th July 2023
Accepted 6th September 2023

DOI: 10.1039/d3ra05114e

rsc.li/rsc-advances

Stealth technology advances in radar-absorbing materials (RAMs) continue to grow rapidly. Barium hexaferrite is the best candidate for RAMs applications. Manganese dioxide (MnO_2) is a transition metal with high dielectric loss and can be used as a booster for changing polarization and reducing reflection loss. The advantages of $BaFe_{12}O_{19}$ and MnO_2 can be combined in a core–shell $BaFe_{12}O_{19}@MnO_2$ composite to improve the material's performance. MnO_2 composition, temperature, hydrothermal holding time, and sample thickness all have an impact on the core–shell structure. In this study, a core–shell $BaFe_{12}O_{19}@MnO_2$ composite is synthesized in two stages: molten salt synthesis to produce $BaFe_{12}O_{19}$ as the core and hydrothermal synthesis to synthesize MnO_2 as the shell. In the hydrothermal synthesis, $BaFe_{12}O_{19}$ and $KMnO_4$ were mixed in deionized water using different mass ratios of $BaFe_{12}O_{19}$ to $KMnO_4$ (1 : 0.25, 1 : 0.5, 1 : 0.75, and 1 : 1). The main goal of the analysis was to figure out how well the hydrothermal synthesis method worked at different temperatures (140 °C, 160 °C, and 180 °C) and holding times (9 h, 12 h, and 15 h). The composite material was subjected to characterization using a vector network analyzer, specifically at thicknesses of 1.5 mm, 2 mm, 2.5 mm, and 3 mm. The hydrothermal temperature and composition ratio of $BaFe_{12}O_{19}:MnO_2$ are the most influential parameters in reducing reflection loss. Accurate control of the parameters makes a $BaFe_{12}O_{19}@MnO_2$ core–shell composite structure with a lot of sheets. The structure is capable of absorbing 99.99% of electromagnetic waves up to a sample thickness of 1.5 mm. The novelty of this study is its ability to achieve maximal absorptions on a sample with minimal thickness through precise parametric control. This characteristic makes it highly suitable for practical applications, such as performing as an anti-radar coating material. $BaFe_{12}O_{19}@MnO_2$ demonstrates performance as a reliable electromagnetic wave absorber material with simple fabrication, producing absorption at C and X band frequencies.

Introduction

The development of electronic device applications continues to advance and provides many conveniences for human life. Many electronic devices employ wireless device technologies and use radar as an EM wave transmitter. However, excessive use of electronic devices generates radiation and electromagnetic (EM) interference that exceeds safe limits, thereby disrupting human health.[1–5] EM wave radiation, including that from microwave ovens, mobile phones, high-speed processors, radar, and satellite communication, can be found on a daily basis. The rapid development of wireless communication technologies has been associated with an increase in public awareness of electromagnetic pollution hazards. The negative impact of electromagnetic pollution on wireless equipment, precise instruments, and military safety necessitates the immediate development of radar-absorbing materials with high efficiency and broadband electromagnetic wave absorption.[6] A microwave absorber material can absorb harmful radiation from EM waves.[7] Stealth technology stems from the steady improvement of science and technology in the military field, continuously improving to enhance the quality of radar absorption and usage thereof. It is an indicator of a country's military strength and is used to guard border areas to avoid infiltration by foreign parties. Foreign vehicles equipped with radar necessitate that

---

[a] *Department of Metallurgical Engineering, Faculty of Engineering, Sultan Ageng Tirtayasa University, Jl. Jend. Sudirman KM 03, Cilegon 42435, Banten, Indonesia. E-mail: erlina.yustanti@untirta.ac.id*

[b] *Center of Excellence, Nanomaterial and Process Technology Laboratory, Faculty of Engineering, Sultan Ageng Tirtayasa University, Jl. Jend. Sudirman KM 03, Cilegon 42435, Banten, Indonesia. E-mail: erlina.yustanti@untirta.ac.id*

[c] *Nano Center Indonesia, Jl. PUSPIPTEK Tangerang Selatan 15314, Banten, Indonesia*

[d] *Department of Mechanical Engineering, Mercu Buana University, Jl. Meruya Selatan, Kebun Jeruk, Jakarta 11650, Indonesia*

[e] *Research Center for Telecommunication, National Research and Innovation Agency, Bandung, Indonesia*

[f] *Department of Physics, Faculty of Mathematics and Natural Sciences, Universitas Negeri Malang, Jl. Semarang No 5 Malang, 65145, Indonesia*

each country owns a technology to avoid radar monitoring. With a view to solving these problems, many researchers thought of camouflaging a defense system's main equipment so that radar could not detect it.

Ferrite is a popular microwave absorption material due to its low production costs and high magnetic permeability. Spinel, granite, and magnetoplumbite are the three crystal formations of ferrite. Because of its high magnetic anisotropy but high density, absorption, and low efficiency, hexagonal magnetoplumite is chosen as the best anti-radar absorbent material.[8] The chemical formula and crystal structure of barium ferrites are classified as M type ($BaFe_{12}O_{19}$), Y type ($BaMe_2Fe_{12}O_{22}$), W type ($BaMe_2Fe_{16}O_{27}$), Z type ($Ba_3Me_2Fe_{24}O_{41}$), X type ($Ba_2Me_2Fe_{28}O_{46}$), and U type ($Ba_4Me_2Fe_{36}O_{66}$). Me is a metal cation with radii that are almost comparable to Fe, resulting in the required engineering materials.[9] Large coercivity fields in barium hexaferrite (BHF) make it unsuitable for use as an absorbent material for microwaves. The coercivity field gets smaller when Fe ions are replaced with other metal cations that have almost the same radius.[10] M-type hexagonal ferrite has been the subject of extensive research and development over the last decades.[11] An M-type hexagonal ferrite material was selected because of its properties as a permanent magnet and because it exhibited the potential to be used as a radar-absorbing material (RAM). The advantages of barium hexaferrite ($BaFe_{12}O_{19}$, *i.e.*, BHF) include a high saturation magnetization value of 72 A m^2 kg^{-1}, a large coercive field of 594 kA m^{-1}, a high Curie temperature of 450 °C, satisfactory corrosion resistance, and chemical stability.[12] However, $BaFe_{12}O_{19}$ suffers weaknesses as an absorber, namely with respect to its high density, narrow absorption band, and high reflection loss. Its permittivity and permeability considerably differ, resulting in impedance mismatching, which results in a nonideal EM absorption performance. An effective strategy to achieve ideal impedance matching is to form a magnetic/dielectric composite structure.[8] Several microstructural designs that can form magnetic or dielectric composites include ultrasonic spray,[13] core–shell,[14] sandwich-like, hollow sphere, porous,[5] and multi-layered.[15] Encapsulating magnetic materials with nonmagnetic ones can also be used to increase energy anisotropy, resulting in increased absorption.[16,17] Nevertheless, achieving a simultaneous realization of high reflection loss (RL), low thickness, and lightweight[18] poses significant challenges for radar-absorbing materials due to the inherent trade-off between impedance match, attenuation capability,[19] and excellent corrosion resistance.[20]

Manganese oxide (MnO_2) is a dielectric material that can be used as a shell because it has multiple valences (Mn^{2+}, Mn^{3+}, and Mn^{4+}), strong oxidizing ability, EM radiation absorption ability based on the structural properties of Mn, a large surface area, acid resistance, low toxicity, a narrow band gap, low cost, and is good for the environment.[21] As an antiradar material, BHF can be synthesized as nanoparticles *via* top–down or bottom–up methods. Generally, for the synthesis of BHF-based nanoparticles, in addition to the hydrothermal method, other alternatives exist, including mechanical alloying,[22–24] coprecipitation,[10,25,26] sol–gel,[27] and autocombustion.[28] Hydrothermal synthesis offers advantages over other synthesis methods: low cost, nontoxicity, environmentally friendly precursors, and simple procedures.

Hydrothermal synthesis of barium hexaferrite with manganese dioxide creates a core–shell composite with a reflection loss of −54.39 dB at 11.26 GHz. Hu *et al.* analyzed the effect of temperature and sample thickness and determined that EM wave absorption was greatest at 170 °C and a thickness of 2.6 mm.[8] The increased composition ratio of MnO_2 on CIP@MnO_2 composites increased impedance matching dielectric loss.[29] In our previous work, $BaFe_{11.2}Mg_{0.4}Al_{0.4}O_{19}$ was fabricated to achieve a reflection loss of −40.8697 dB at 11.896 GHz.[24] The effect of Mg–Al substitution increasing electromagnetic wave absorption of $BaFe_{12-2x}Mg_xAl_xO_{19}$ with reflection loss of −17.62 dB at 8.2 GHz[23] and fabrication of $BaFe_9Mn_{1.5}Ti_{1.5}O_{19}$, which achieved reflection loss of −19.75 dB at 13.6 GHz.[22] Lin *et al.* prepared the $BaFe_{12}O_{19}$@Fe_3O_4 core–shell composite, which achieved the reflection loss of −33,6 dB.[30] Liu *et al.* prepared $BaFe_{12}O_{19}$@C with the reflection loss of −87.41 dB at 10.72 GHz.[31] Lu *et al.* prepared $BaFe_{12}O_{19}$@$ZnFe_2O_4$/$MWCNT_S$, which achieved the reflection loss of −42.35 dB.[32] In light of the previous study, additional investigation was undertaken to examine the impact of alterations in hydrothermal holding time, temperature, $BaFe_{12}O_{19}:MnO_2$ mass ratio composition, and sample thickness on enhancing the performance of radar-absorbing materials at minimum sample thickness.

The novelty of this research is in the control of the BHF : MnO_2 composition ratio, which has not been previously investigated. It will be interesting to see how this affects the reduction of reflection loss. Some previous researchers focused more on hydrothermal temperature variations and made little study of hydrothermal holding time to reduce reflection loss. Controlling the appropriate $BaFe_{12}O_{19}$@MnO_2 synthesis parameters makes a nanoflower MnO_2 structure with flattened sheets, tight sheets, and enough sheet depth to absorb the most electromagnetic radiation. The research involved the development of anti-radar-property-containing coatings with narrow thicknesses to facilitate practical application. The research objective produced the thinnest anti-radar material that was readily applicable as a coating. This study looks at how to improve microwave absorption performance up to 99.99% in wideband C and X band frequencies by changing sample composition, hydrothermal temperature, hydrothermal holding time, and sample thickness.

Materials and methods

The chemicals used in this study were barium chloride dihydrate ($BaCl_2\cdot 2H_2O$, Merck, purity: ≥99.9%, Darmstadt, Germany), iron(III) oxide (Fe_2O_3, Sigma-Aldrich, purity: ≥99.9%, Saint Louis, MO, USA), barium carbonate ($BaCO_3$, Merck, purity: ≥99.9%, Darmstadt, Germany), potassium permanganate ($KMnO_4$, Mallinckrodt, purity: ≥99.5%, St. Louis, Missouri, USA), and sodium chloride (NaCl, Pudak-Scientific, purity: ≥99.9%, Bandung, Indonesia).

The synthesis of $BaFe_{12}O_{19}$ in molten salt began with the stoichiometric mixing of $BaCO_3$, Fe_2O_3, and NaCl at a $BaFe_{12}O_{19}$: NaCl mass ratio of 1 : 2. The precursors were milled at

150 rpm in a planetary ball for 2 h in an ethanol medium. Subsequently, the milled samples were dried at 80 °C for 12 h and then calcined at 1000 °C for 2 h. The next step was to rinse the sample to remove the salt content. In the second molten salt step, mix with a $Fe_2O_3 : BaCl_2{\cdot}2H_2O$ mass ratio of 1 : 2 to form $BaFe_{12}O_{19}$ and a $BaFe_{12}O_{19} : Fe_2O_3$ molar ratio of 1 : 500. The samples were dried at 80 °C for 12 h, followed by calcination at 1100 °C for 8 h in a muffle furnace.

The synthesis of the $BaFe_{12}O_{19}$@MnO_2 core–shell composite started with dissolving $KMnO_4$ in deionized water and adding in $BaFe_{12}O_{19}$ at various $BaFe_{12}O_{19} : KMnO_4$ mass ratios (1 : 0.25, 1 : 0.5, 1 : 0.75, and 1 : 1). The homogeneous sample solution was placed into a Teflon-lined autoclave vessel at various hydrothermal temperatures (140 °C, 160 °C, and 180 °C) with holding times of 9 h, 12 h, and 15 h. Table 1 presents the details of the sample code parameters. Fig. 1 shows the research design.

X-ray diffraction (XRD) characterization was performed to determine the crystal structure (Bruker D8 Advance, Massachusetts, USA). We used a Cu tube operated at 40 kV/35 mA, 280 mm goniometer radius, 0.6 divergence slit, 2.5 soller slit at 5° min^{-1}, with a range of 2-theta 20°–100°.

The surface microstructure and morphology were analyzed *via* field emission scanning electron microscopy with electron-dispersive X-ray spectrometry (FESEM-EDS, JIB-4610 F, JEOL, Tokyo, Japan) operated at 15 kV accelerating voltage. The particle size distribution was analyzed *via* particle size analysis (PSA Malvern Zetasizer). The magnetic properties were studied using a vibrating sample magnetometer (VSM250, Xiamen, China). A vector network analyzer (VNA, two ports, Anritsu MS 46322 A, Allen, TX, USA) was used to analyze the *S* parameters in a bid to estimate the transmission and RLs. Reflection loss by eqn (1) and (2)[6,33–37] were used to calculate the RL *via* the Nicholson–Ross–Weir method, employing measurements of the transmission signal (S21) and reflection signal (S11).

$$\mathrm{RL(dB)} = 20\ \log\left|\frac{Z_{\mathrm{in}} - Z_{\mathrm{o}}}{Z_{\mathrm{in}} + Z_{\mathrm{o}}}\right| \tag{1}$$

$$Z_{\mathrm{in}} = Z_{\mathrm{o}}\sqrt{\frac{\mu_{\mathrm{r}}}{\varepsilon_{\mathrm{r}}}}\tanh\left[\left(j\frac{2\pi fd}{c}\right)\sqrt{\mu_{\mathrm{r}}\varepsilon_{\mathrm{r}}}\right] \tag{2}$$

Z_{in} and Z_{o} represent the impedances of the material and free space: relative permittivity (ε_{r}), relative permeability (μ_{r}), velocity of light in a vacuum (*c*), EM frequency (*f*), and sample thickness (*d*).

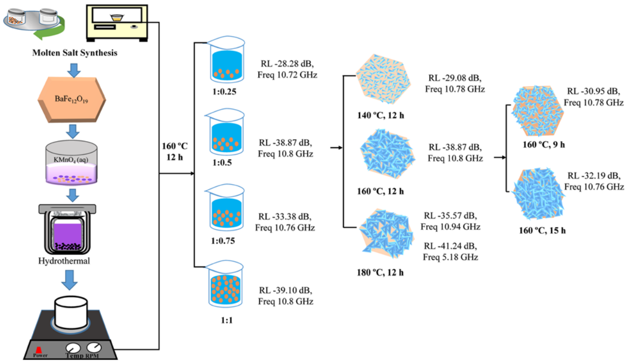

Fig. 1 The hydrothermal synthesis of $BaFe_{12}O_{19}$@MnO_2.

Results and discussion

Crystal structure of the $BaFe_{12}O_{19}$@MnO_2 core–shell composite

The identification of the diffraction pattern of hydrothermally synthesized $BaFe_{12}O_{19}$@MnO_2 at mass ratios of 1 : 0.25, 1 : 0.5, 1 : 0.75, and 1 : 1 is shown in Fig. 2. Single-phase BHF successfully obtained matches with reference Crystallography Open Database (COD) CIF 9008137.

The peak characteristics of $BaFe_{12}O_{19}$ were marked at 22.9°, 30.3°, 32.1°, 34.1°, 37.1°, 55°, 56.5°, and 63°, corresponding to the *hkl* planes (006), (110), (017), (114), (023), (127), (0211), and (220), respectively. $BaFe_{12}O_{19}$ crystals have a hexagonal structure with a *P*6$_3$/*mmc* space group. The peak characteristics of MnO_2 confirmed by ICSD number 98-007-6430 were marked at 37.2°, 42.7°, 56.5°, and 67.1°, corresponding to the *hkl* planes (010), (011), (012), and (110), respectively. MnO_2 crystals have a hexagonal structure with a *P*6$_3$/*mmc* space group. Rietveld refinement of the diffraction pattern was performed using the software material analysis using diffraction (MAUD). The refinement parameters included background, scale factor, atomic positions, lattice parameters, and crystal orientation. Refinement results were accepted if they met the reliability index values of the *R*-weighted profile (R_{wp}), *R*-expected profile (R_{exp}), and SIG. In the MAUD program, the SIG parameter is

Table 1 Parameters of the sample code design

			Hydrothermal	
Sample code	Ratio wt% (BHF : MnO_2)	Sample thickness (mm)	Temperature (°C)	Holding time (hours)
A	1 : 0.25	1; 1.5; 2; 2.5; 3	160	12
B	1 : 0.5	1; 1.5; 2; 2.5; 3	160	12
C	1 : 0.75	1; 1.5; 2; 2.5; 3	160	12
D	1 : 1	1; 1.5; 2; 2.5; 3	160	12
E	1 : 0.5	1; 1.5; 2; 2.5; 3	140	12
F	1 : 0.5	1; 1.5; 2; 2.5; 3	180	12
G	1 : 0.5	1; 1.5; 2; 2.5; 3	160	9

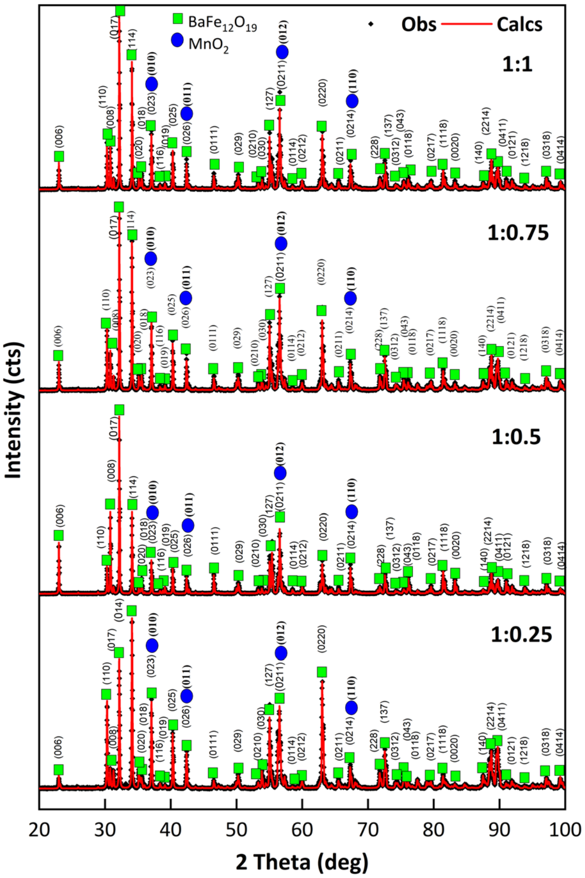

Fig. 2 Diffraction patterns of BaFe$_{12}$O$_{19}$@MnO$_2$ synthesized at various BaFe$_{12}$O$_{19}$: MnO$_2$ mass ratios.

used to judge how well crystal structure models made from X-ray diffraction patterns match reality. SIG is the standard deviation between the calculated and observed intensities within the range. This parameter is a measure of the suitability between observed and calculated diffraction patterns. Parameter values are expected to change during refinement. The smaller the reliability index, the higher the agreement between observed and calculated diffraction patterns. Refinement is accepted if it meets a SIG of 4, R_{wp} of 20%, and R_{exp} of 15%. The diffraction pattern resulting from the XRD characterization was refined by comparing it to the standard COD diffraction pattern CIF-9008137. The CIF-9008137 data have space group of $P6_3/mmc$ with a hexagonal crystal system, and the lattice parameters a and c are 5.893 Å and 23.194 Å, respectively.

At different BaFe$_{12}$O$_{19}$: MnO$_2$ mass ratios (1 : 0.25, 1 : 0.5, 1 : 0.75, and 1 : 1), the results of samples A, B, C, and D were shown in Fig. 2 and Table 2. Single-phase BaFe$_{12}$O$_{19}$@MnO$_2$ was successfully synthesized (see Table 2's outcomes of the refinement). Table 2 presents the result of BaFe$_{12}$O$_{19}$@MnO$_2$ refinement using the software MAUD at various BaFe$_{12}$O$_{19}$: MnO$_2$ mass ratios with highly satisfactory validation. In general, the intensity of the diffraction pattern decreases as the mass fraction of MnO$_2$ in the BaFe$_{12}$O$_{19}$@MnO$_2$ composite material increases. It has been suggested that the observed reduction in intensity can be attributed to the agglomeration of MnO$_2$, creating a covering on the surface boundary of BaFe$_{12}$O$_{19}$. Consequently, there is a tendency for the crystallite size of BaFe$_{12}$O$_{19}$@MnO$_2$ to increase slightly.[29,38–40] Through careful control of the synthesis parameters, MnO$_2$ agglomeration can be minimized. This is in line with the FESEM result that MnO$_2$ has the perfect structure of a nanoflower. Thus, the increase in BaFe$_{12}$O$_{19}$@MnO$_2$ crystallite size is not significant, as shown in Table 2.

The lattice parameters and unit-cell volume of BaFe$_{12}$O$_{19}$@MnO$_2$ experienced a small drop as the mass fraction of MnO$_2$ increased. The substitution of the Fe^{3+} ion (0.64) with the

Table 2 Rietveld refinement of BaFe$_{12}$O$_{19}$@MnO$_2$ at various BaFe$_{12}$O$_{19}$: MnO$_2$ mass ratios

Description	1 : 0.25 (A)	1 : 0.5 (B)	1 : 0.75 (C)	1 : 1 (D)
SIG	2.0892	2.0053	2.1409	2.1081
R_{wp} (%)	16.73	15.61	14.518	15.035
R_{exp} (%)	8.0082	7.7843	6.7813	7.1321
a (Å)	5.8939	5.8936	5.8934	5.8931
c (Å)	23.2045	23.1991	23.1984	23.1981
Volume (Å^3)	697.878	697.753	697.657	697.598
Density (g cm^{-3})	5.29	5.29	5.29	5.29
Crystallite (nm)	59.18	59.17	59.19	59.22

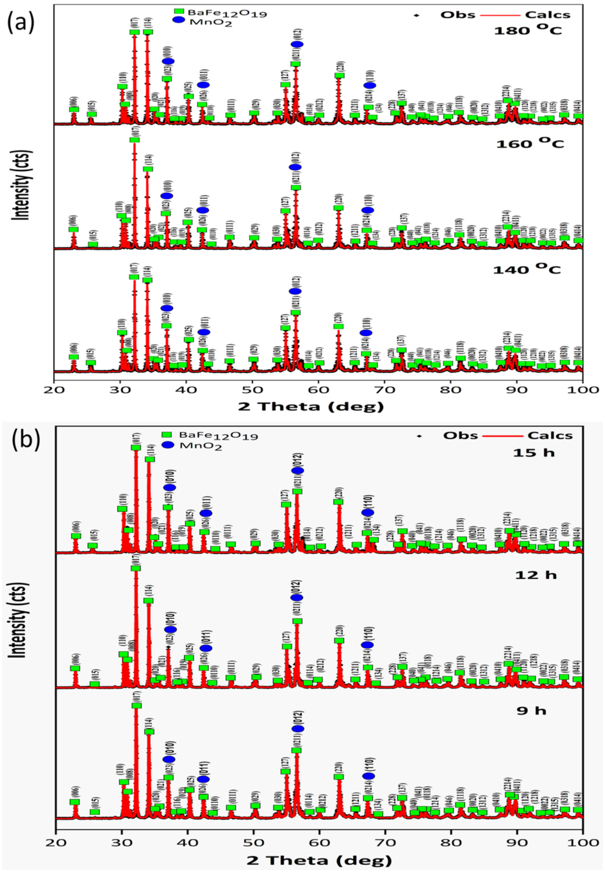

Fig. 3 Diffraction patterns of BaFe$_{12}$O$_{19}$@MnO$_2$ synthesized at various hydrothermal (a) temperatures and (b) holding times.

Table 3 Rietveld refinement of $BaFe_{12}O_{19}@MnO_2$ at hydrothermal temperatures and holding times

Description	140 °C, 12 h	160 °C, 12 h	180 °C, 12 h	160 °C, 9 h	160 °C, 15 h
SIG	2.184	2.108	2.446	2.618	1.853
R_{wp} (%)	18.125	15.035	19.006	18.647	13.446
R_{exp} (%)	7.116	7.132	6.819	7.122	7.254
a (Å)	5.8932	5.8931	5.8936	5.8933	5.8930
c (Å)	23.1974	23.1984	23.1975	23.1960	23.1970
Volume (Å^3)	697.591	697.598	697.679	697.607	697.681
Density (g cm^{-3})	5.290	5.290	5.290	5.290	5.290
Crystallite size (nm)	57.800	59.220	65.580	44.480	69.580

Mn^{4+} ion (0.53) resulted in a decrease in the lattice parameters. However, the density remained unchanged as the addition of Mn had already been accounted for in the mass. The utilization of Mn^{4+} in replacement of Fe^{3+} results in a decrease in the lattice parameters and unit-cell volume. The reason for this is that Mn^{4+} has a relatively smaller atomic radius in comparison to Fe^{3+}.[41]

Fig. 3 shows the XRD diffraction pattern obtained when the mass ratio of $BaFe_{12}O_{19}$ to MnO_2 is 1 : 0.5. Fig. 3(a) shows samples E, D, and B synthesized at variations in hydrothermal temperature (140 °C, 160 °C, and 180 °C) for a holding time of 12 h. Fig. 3(b) shows samples G, B, and H at variations in hydrothermal holding time (9 h, 12 h, and 15 h) at a temperature of 160 °C. The rise in hydrothermal temperature increases the intensity of the diffraction peaks, which indicates an increase in crystallinity. Rising hydrothermal temperature increases the crystallite size owing to an increased reaction rate. During the hydrothermal process, hydrothermal temperature and holding time have the same effect on increasing the crystallite size because both of these parameters affect the rate of synthesis and decomposition of precursors[42] in the endothermic reaction of $BaFe_{12}O_{19}@MnO_2$ synthesis.

Using the established standard (see Table 3), the SIG, R_p, and R_{exp} values show how well the calculated and observed diffraction patterns match (based on the modeling data). The holding time affects the intensity of the resulting diffraction pattern. The greater the holding time, the higher the diffraction pattern's intensity, so that the compatibility between calculated and observed diffraction patterns is maximized. From Table 2, it can be seen that the increase in the mass fraction of MnO_2 did not affect the crystallite size of $BaFe_{12}O_{19}@MnO_2$. However, an increase in temperature and hydrothermal holding time increased the crystallite size.

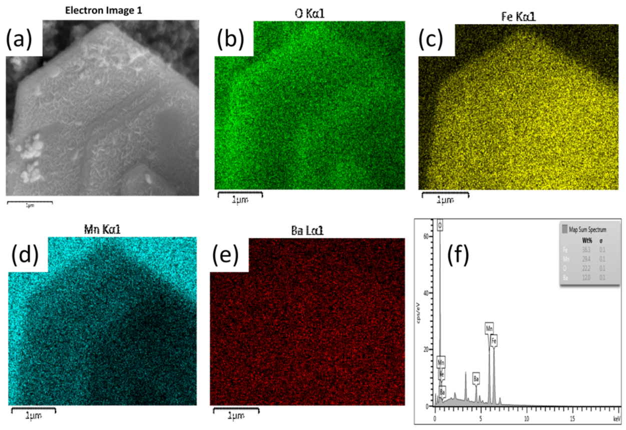

Fig. 4 (a) FESEM image of the $BaFe_{12}O_{19}@MnO_2$; (b–e) EDS mapping of the $BaFe_{12}O_{19}$@; and (f) element content of the $BaFe_{12}O_{19}@MnO_2$.

Field emission scanning electron microscopy results

Fig. 4 shows the results of the EDS elemental mapping, which shows how the elements in $BaFe_{12}O_{19}@MnO_2$ are spread out based on the difference in color spectrum. The elemental mapping results demonstrate that Mn is uniformly distributed in $BaFe_{12}O_{19}$. The core–shell $BaFe_{12}O_{19}@MnO_2$ composite was successfully synthesized and homogeneous. The EDS mapping results show that the composition of the constituent elements of $BaFe_{12}O_{19}@MnO_2$ was 3.4% Ba, 24.4% Fe, 52.1% O, and 20.1% Mn. The elemental content of Mn is evenly distributed in $BaFe_{12}O_{19}$, and Mn addition can enhance the magnetic and dielectric properties, thereby increasing the absorption of EM waves.[8,40,43]

Fig. 5(a–f) show the structure of the MnO_2 core cell resulting from hydrothermal synthesis at various compositions, temperatures, and hydrothermal holding times at magnifications of 500 00× and 1 500 00×. Fig. 5(g–l) shows the success of molten salt synthesis at making MnO_2 attachment pathways on the surface of BHF at different BHF : MnO_2 mass ratios, hydrothermal temperatures, and hydrothermal holding times at 300 00× and 1 000 00× magnifications. Generally, the BHF structure has a morphology with a highly smooth surface without any pores on the surface.

Fig. 5(a, b, g and h) shows the morphology for various BHF : MnO_2 mass ratios (1 : 0.25 and 1 : 0.5) at 160 °C for 12 h of holding time. An increase in the MnO_2 fraction affects the distribution and results in MnO_2 agglomeration on the surface of $BaFe_{12}O_{19}$, which agrees with previous studies.[3] Fig. 5(a and b) show the size of the nanoflower MnO_2; the thicker the petals, the higher the particle size (see Fig. 6(a)). From Fig. 5(g and h), it can be seen that increasing the fraction of MnO_2 in $BaFe_{12}O_{19}@MnO_2$ provides a pathway for the growth of more MnO_2 nanoflowers.

Fig. 5(b–d and h–j) shows results for temperature (160 °C, 140 °C, and 180 °C) with a 12 hour holding time. The increase in hydrothermal temperature aims to result in more nucleation of the core and cell in the $BaFe_{12}O_{19}@MnO_2$ composite system.[8]

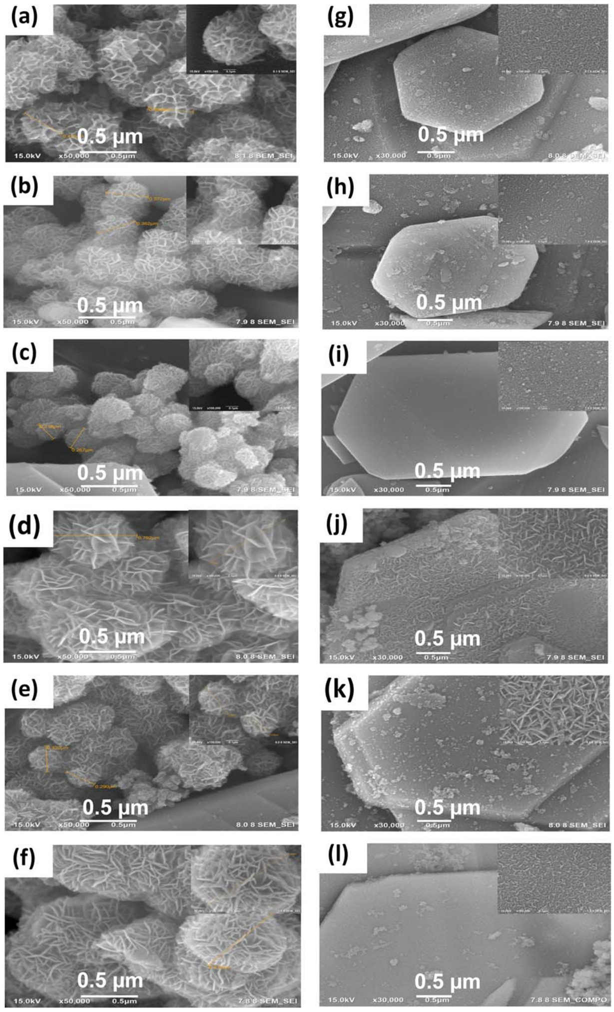

Fig. 5 FESEM image of $BaFe_{12}O_{19}@MnO_2$ (a and g) mass ratio of 1 : 0.25; (b and h) mass ratio of 1 : 0.5; (c and i) temperature of 140 °C; (d and j) temperature of 180 °C; (e and k) holding time 9 h; (f and l) holding time 15 h.

Fig. 5(c) and (i) show the structure of MnO_2 nanoflower small sheets with the smallest particle diameter and the valley shape of the MnO_2 sheets, which wasn't seen at 140 °C. Although the maximum magnification is 1 500 00×, the formation of MnO_2 flowers is imperfect. On the surface of the hexagonal BHF, there are indications of fine strokes overlapping each other at 300 00× and 1 000 00× magnifications. The hydrothermal synthesis mechanism has a lower reaction rate when conducted at lower temperatures, resulting in isotropic crystal growth. Inversely, higher temperatures lead to an increased reaction rate, causing the aggregation of MnO_2 crystals with anisotropic growth.[44] Previous studies showed that $BaFe_{12}O_{19}$ produced using molten salt had a size in the range of 25–50 µm,[40,45] while MnO_2 nanoflowers had a size in the range of 200–600 nm.[5,46] The MnO_2 nanoflower exhibits a particle size of 792 nm at a temperature of 180 °C, as depicted in Fig. 5(d and j). Conversely, at a temperature of 160 °C, the particle size decreases to 365 nm, as shown in Fig. 5(b and h). The smallest particle size of 232.5 nm is observed at the lowest temperature of 140 °C, as illustrated in Fig. 5(c and i). The changing of hydrothermal temperature has a significant impact on both the particle size of MnO_2 and the surface area of barium hexaferrite.[47] The particle size and depth of the nanosheets grew with increasing hydrothermal temperature, as shown in Fig. 5(c, d, i and j), and the MnO_2 route on the surface of $BaFe_{12}O_{19}$ rose maximally at 160 °C. The FESEM characterization revealed that the diameter of the nanoflowers increased with increasing temperature in the hydrothermal synthesis. The larger the surface area of the nanoflower, the greater the EM wave absorption on the absorber material. Shell thickness plays a crucial part in the ongoing absorption process by lowering wave reflection, boosting EM wave scattering, and offering an opportunity to attenuate EM waves more effectively. A recent study found that a hydrothermal temperature of 170 °C with a holding time of 12 hours was ideal for the creation of more homogeneous nanoflowers.[8]

The growth of MnO_2 and BHF particles is affected by hydrothermal temperature and holding time. Fig. 5(e and k) shows that a holding time of 9 h results in the growth of nanoflowers with a 284.66 nm particle size, short MnO_2 sheet segments, and considerably thin BHF surface stripes. In Fig. 5(d and j), a holding time of 12 h results in a uniform particle size of 792 nm and a larger, wider sheet. The boundaries between the flowers are marked with the edges of the sheet on the

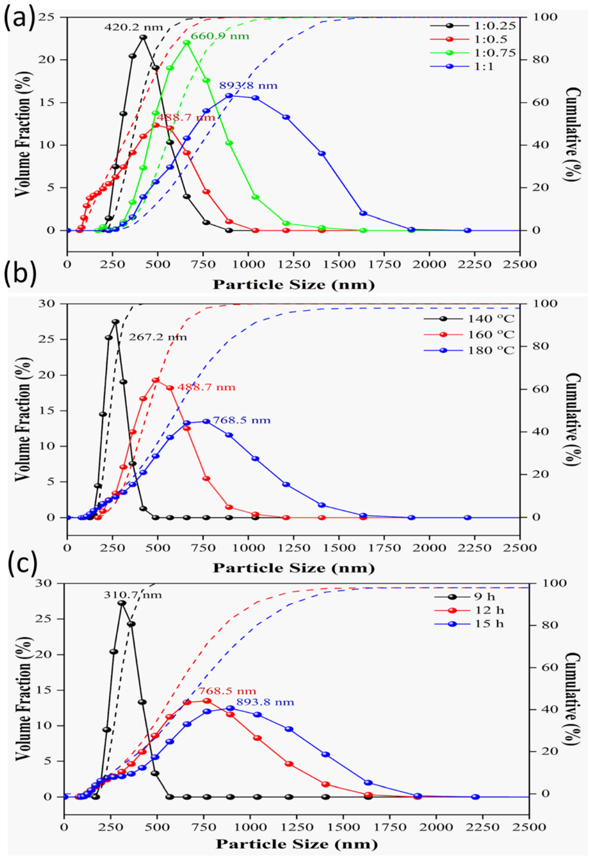

Fig. 6 PSA results for $BaFe_{12}O_{19}@MnO_2$ (a) mass ratio, (b) temperature, and (c) hydrothermal holding time.

nanoflower, which are more pronounced, showing the difference between the upper (lighter in color) and inner parts (dark in color) of the sheets. From Fig. 5(f and l), it can be seen that a holding time of 15 h results in the largest MnO_2 nanoflower size, *i.e.*, 800 nm. In the high-temperature hydrothermal synthesis of $BaFe_{12}O_{19}$@MnO_2, the structure of the nanosheet shells in MnO_2 appears flat with a larger size and thickness.[47] The morphology of the increasing number of MnO_2 nanosheets can be controlled by increasing the holding time in the hydrothermal synthesis of $BaFe_{12}O_{19}$@MnO_2. The scanning electron microscopy characterization results show increased homogeneity in sample morphology, agreeing with a previous study.[48] Increasing the hydrothermal holding time did not considerably change the size of the MnO_2 particles but increased the dispersion and uniformity of the particles to make them more homogeneous, in line with a previous study.[49] Maximum EM wave absorption is not guaranteed by the small particle size. However, a core–shell composite with the highest performance is created by the hexagonal plate-like BHF microstructure, where the surface is covered by the MnO_2 nanoflower growth pathway. The MnO_2 nanoflower exhibits a maximum polarization effect due to its enormous number, high density, and depth of sheets. The MnO_2 nanoflower structure exhibits a scattering effect as a result of the composite core–shell construction, which considerably reduces reflection loss.

Particle size analyzer

The size of the particles and crystallites also influences EM wave absorption. Notably, EM wave absorption rises as particle and crystallite sizes decrease. Small particles have a wide surface area, which increases EM wave absorption by magnetic dipole moment.[24] The size of $BaFe_{12}O_{19}$@MnO_2 particles rises with increasing MnO_2 fraction in BHF, as shown in Fig. 6(a).

Fig. 6(b) demonstrates that the findings of this investigation are compatible with those of a prior study, which found that the particle size of MnO_2 nanoflowers is in the 200–600 nm range.[5,46] Temperature and hydrothermal holding time were found to increase particle size by up to 288% in this investigation. However, increasing the MnO_2 fraction resulted in a 213% increase in particle size. Increases in temperature and hydrothermal holding time enhanced the crystallite size of $BaFe_{12}O_{19}$@MnO_2 from 57.80 to 69.58 nm, as shown in Table 2.

The fabrication of nanoparticles using hydrothermal synthesis leads to the formation of highly crystalline structures. The size distribution of the particles can be controlled by carefully choosing the composition of the precursor and adjusting synthesis parameters, including temperature, pressure, and reaction duration.[50] The particle sizes determined by FESEM differ slightly from those determined by PSA. At various hydrothermal temperatures of 140 °C, 160 °C, and 180 °C, the particle sizes determined by FESEM were 232.5 nm, 365 nm, and 792 nm, respectively, whereas those determined by PSA were 267.2 nm, 488.7 nm, and 768.5 nm. Particle sizes determined by FESEM characterization were 284.66 nm, 792 nm, and 800 nm for various hydrothermal holding durations of 9 h, 12 h, and 15 h, respectively, while they were 310.7 nm, 768.5 nm, and 893.8 nm for PSA characterization. The slight difference in measurement results between FESEM and PSA instruments is due to the PSA characterization mechanism being based on Brownian motion, which has measurement limitations because the measured particles have a hydrodynamic diameter with the assumption that the hydrodynamic radius is considered spherical without taking into account the hexagonal shape of $BaFe_{12}O_{19}$ particles.

The polydispersity index (PI) is used to estimate the particle size distribution range and to detect aggregation.[51] This study's polydispersity measurement provided a PI of 0.5, showing that the core–shell composite $BaFe_{12}O_{19}$@MnO_2 has a hexagonal, plate-like structure as a base reinforced with MnO_2, with a tendency for generating spherical nanoflowers. As demonstrated in Fig. 5(a and b), the size difference between the core and shell in the core–shell composite results in a bimodal particle size distribution pattern; hexagonal $BaFe_{12}O_{19}$ has a larger size distribution than nanoflowered MnO_2.

Magnetic properties of $BaFe_{12}O_{19}$@MnO_2

Fig. 7(a) shows the results of the VSM characterization as a $BaFe_{12}O_{19}$@MnO_2 hysteresis loop for different $BaFe_{12}O_{19}$: MnO_2 mass ratios (1 : 0.25, 1 : 0.5, 1 : 0.75, and 1 : 1). An increased MnO_2 mass fraction in $BaFe_{12}O_{19}$@MnO_2 results in

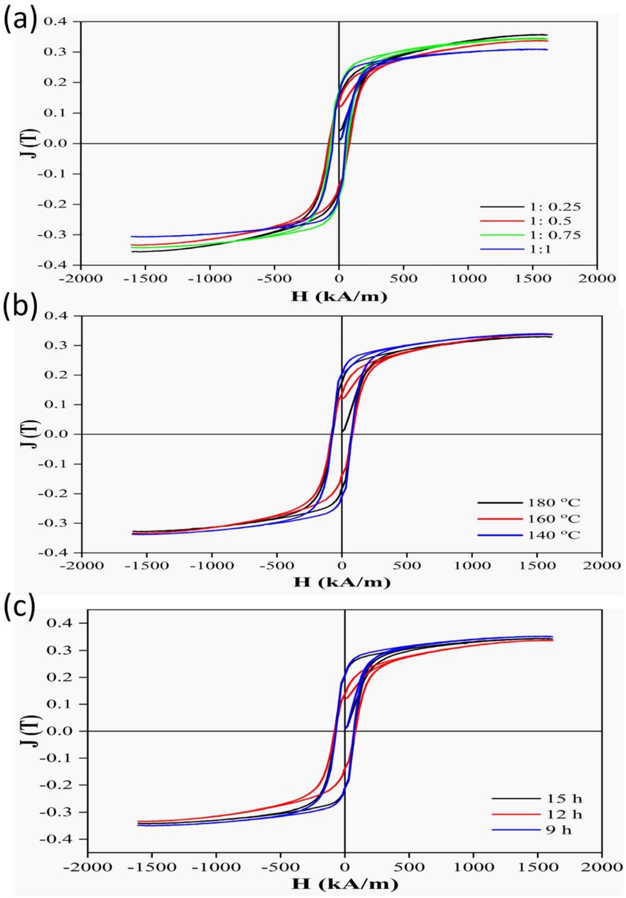

Fig. 7 $BaFe_{12}O_{19}$@MnO_2 VSM results at variations of (a) mass ratio composition, (b) temperature, and (c) hydrothermal holding time.

Table 4 Vibrating sample magnetic characterization of $BaFe_{12}O_{19}$@-MnO_2 at various mass ratio compositions

Sample	M_s (Tesla)	M_r (Tesla)	H_c (kA m^{-1})	BH_{max} (kJ m^{-2})
1 : 0.25	0.3562	0.1449	783.475	41.792
1 : 0.5	0.3432	0.1699	654.781	36.992
1 : 0.75	0.3332	0.1699	652.469	57.395
1 : 1	0.3075	0.1613	507.605	51.732

lower saturation magnetization and coercivity, indicating a transition from a hard to a soft magnet. Fig. 7(b) illustrates that increasing the hydrothermal temperature reduces saturation, coercivity, and BH_{max}. Fig. 7(c) depicts the findings for different hydrothermal holding times (9, 12, and 15 h). Barium hexaferrite is a hard magnet having a total magnetization of 0.47 T, an anisotropic constant of 325 kJ m^{-3}, a Currie temperature of 457 °C, and a resistivity of 10 6 Ωm. Its anisotropic hexagonal structure produces a coercivity field in the range between 1200 and 1300 kA m^{-1}.[52] Previous research showed that BHF, as a hard magnet, has a saturation value of 72 emu g^{-1} and coercivity in the range of 159–255 kA m^{-1}.[53,54] Soft magnets have a coercivity lower than 100 kA m^{-1}, a saturation magnetization in the range of 0.2–1.5 T, and a flat and narrow magnetic loop. Hard magnets have coercivity in the range of 80–400 kA m^{-1}, saturation magnetization in the range of 0.8–2 T, and a wide magnetic loop.[55,56]

In earlier studies,[57] the magnetic saturation and coercivity of the field decreased with increasing mass ratios of MnO_2. From Table 4, it can be seen that upon increasing the mass ratio of MnO_2 in $BaFe_{12}O_{19}:MnO_2$ (1 : 0.25, 1 : 0.5, 1 : 0.75, and 1 : 1), the magnetic saturation decreased from 0.3562 T to 0.3075 T, magnetization remanence slightly increased from 0.1449 T to 0.1699 T, and coercivity reduced from 78.3475 kA m^{-1} to 50.7605 kA m^{-1}. Simultaneously, BH_{max} was slightly increased from 3.6992 kJ m^{-2} to 5.1732 kJ m^{-2}.

The addition of MnO_2 to $BaFe_{12}O_{19}$ successfully changed $BaFe_{12}O_{19}$ from a hard magnet to a soft one, as characterized by a coercivity of 65–78 less than 100 kA m^{-1}. Magnetic saturation and coercivity can decrease with an increasing MnO_2 fraction. Past research works[57–59] emphasized that because MnO_2 is antiferromagnetic, its spin results in a decrease in surface anisotropy, reducing the spin magnetic moment. The remanence increased with the MnO_2 fraction, which was possible because Fe^{3+} ions occupy BHF crystals in the octahedral, tetrahedral, and trigonal bipyramidal lattices. A downward spin was observed in the tetrahedral (4f1) and octahedral (4f2) lattices, which enhanced the material's magnetic characteristics. However, the octahedral (12 k, 2*a*) and trigonal bipyramidal (2*b*) lattices had an upward spin, deteriorating the material's magnetic characteristics. Mn^{4+} of MnO_2 can replace Fe^{3+} on 4f1 and 4f2, increasing the remanence.

From Table 5, it can be seen that increasing hydrothermal temperature decreases the saturation, remanence, BH_{max}, and coercivity of the magnetic field, agreeing with previous research works.[60] It can also be seen that an increase in hydrothermal temperature up to 160 °C in the synthesis of $BaFe_{12}O_{19}$@MnO_2 results in a lower BH_{max}. It seems that the effect of particle energy leads to a wider continuous excitation spectrum, while at 140 °C, the magnetization value goes up because Fe^{3+} spin collinearity goes up in nanoparticles. At 140 °C, thermal fluctuations are reduced to produce an isotropic magnetic moment, and these conditions increase the coercivity field.[60] A hydrothermal temperature of 180 °C with a holding time of 12 h results in the lowest magnetic saturation and BH_{max}, as presented in Table 5.

In the synthesis of antiradar materials, magnetic components are crucial to ensuring the effectiveness of EM wave absorption. The magnetic component will affect the magnetic dipole moment, where the magnetic dipole moments will interact, and there is a high possibility of a transition from a low-to high-energy level. On a microscopic level, the way EM waves are absorbed is due to interactions between magnetic dipoles, which change the potential energy depending on how far apart each magnetic dipole moment is. This difference in potential energy causes the microwaves to be absorbed in various ways. Based on this, it can be said that the MnO_2 doping mechanism changed the essential properties of $BaFe_{12}O_{19}$ from those of a hard magnet to those of a soft magnet. This is shown by the fact that the coercivity changed by less than 100 kA m^{-1}. Reducing the properties of a hard magnet to those of a soft magnet might decrease the instances of loss of magnetic resonance of BHF as a RAM.[61]

Study of the vector network analysis

In this study, one of the most important ways to measure EM waves that could still be correlated is through vector network analysis and characterization. The EM waves that reach the antiradar material $BaFe_{12}O_{19}$@MnO_2 can be absorbed, deflected, or reflected. By adding the dopant MnO_2 to $BaFe_{12}O_{19}$ and changing the mass ratio of MnO_2 to $BaFe_{12}O_{19}$, temperature,

Table 5 VSM results of $BaFe_{12}O_{19}$@MnO_2 at various temperatures and holding times

Temperature and holding time	M_s (Tesla)	M_r (Tesla)	H_c (kA m^{-1})	BH_{max} (kJ m^{-2})
180 °C, 12 h	0.3207	0.1753	728.804	32.218
160 °C, 12 h	0.3432	0.1699	654.781	36.992
140 °C, 12 h	0.3562	0.1449	783.475	39.876
160 °C, 15 h	0.3425	0.2076	780.657	36.891
160 °C, 12 h	0.3432	0.1699	654.781	36.937
160 °C, 9 h	0.3514	0.2069	705.488	38.794

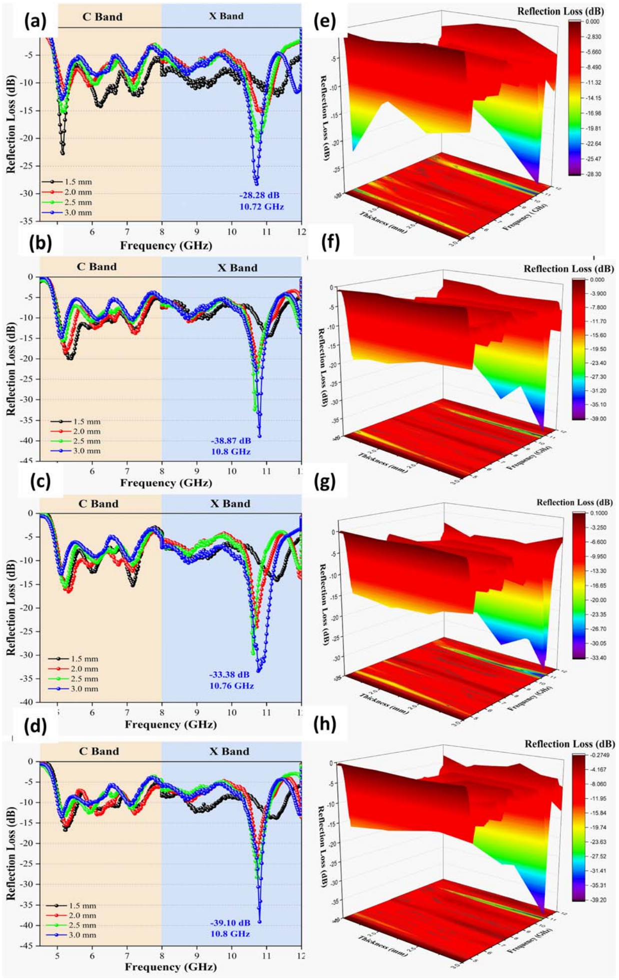

Fig. 8 RL of $BaFe_{12}O_{19}$@MnO_2 at 4–12 GHz frequency with different (a–d) mass ratios (0.25–1.0) and (e–h) 3D representations.

and hydrothermal holding time, it is possible to get the most microwave absorption with the least amount of waves being deflected and reflected. In this study, VNA characterization was done in the C and X bands to guarantee the performance of $BaFe_{12}O_{19}$@MnO_2 as a radar-absorbing material.

The RL decreased with increasing fractions of MnO_2 in $BaFe_{12}O_{19} : MnO_2$, as shown in Fig. 8(a–d). The observed shift in MnO_2 mass ratio occurs at 10.82 GHz, resulting in a 38.26% decrease in reflection loss from −28.28 dB to −39.10 dB. The observed change in the mass ratio of MnO_2 occurs at a frequency of 10.82 GHz, resulting in a reduction in reflection loss of 38.26% from −28.28 dB to −39.10 dB. These findings suggest that there was a significant increase in microwave absorption, with the absorption rate rising up to 99.99%. Increasing the MnO_2 fraction effectively reduced RL on account of the impedance-matching effect, agreeing with previous research.[29,62] Previous studies reported that enhancing the material's dielectric properties effectively reduced RL owing to impedance-matching conditions.[40,63]

Engineering of BHF nanoparticles with MnO_2 forms a core–shell nanocomposite structure, combining their magnetic and dielectric loss characteristics to fabricate a superior absorber material. Dielectric materials offer the advantages of high dissipation ability and satisfactory stability. The synergistic effect between magnetic and dielectric losses can enhance EM absorption performance.[5,31,43] A core–shell composite is a microstructure that has a synergistic effect between the core and shell owing to interfacial polarization originating from the accumulation of charges and ions at the interface, contributing to increased absorption.[17] The conjugation between the magnetic and dielectric materials results in impedance matching, thereby increasing EM absorption and energy dissipation.

Fig. 8(a–d) shows that a sample with a maximum thickness of 3 mm always produces a minimum RL. The lowest RL was obtained at 1 : 1 mass ratio and 3 mm thickness, *i.e.*, −39.10 dB (10.8 GHz; 99.99% absorption). This observation indicates a positive correlation between sample thickness and microwave absorption, suggesting that greater absorption of microwaves by the antiradar material leads to a decrease in reflection loss.[64]

Fig. 9(a–c) shows increased hydrothermal temperature decreases reflection loss; when compared to other factors, the

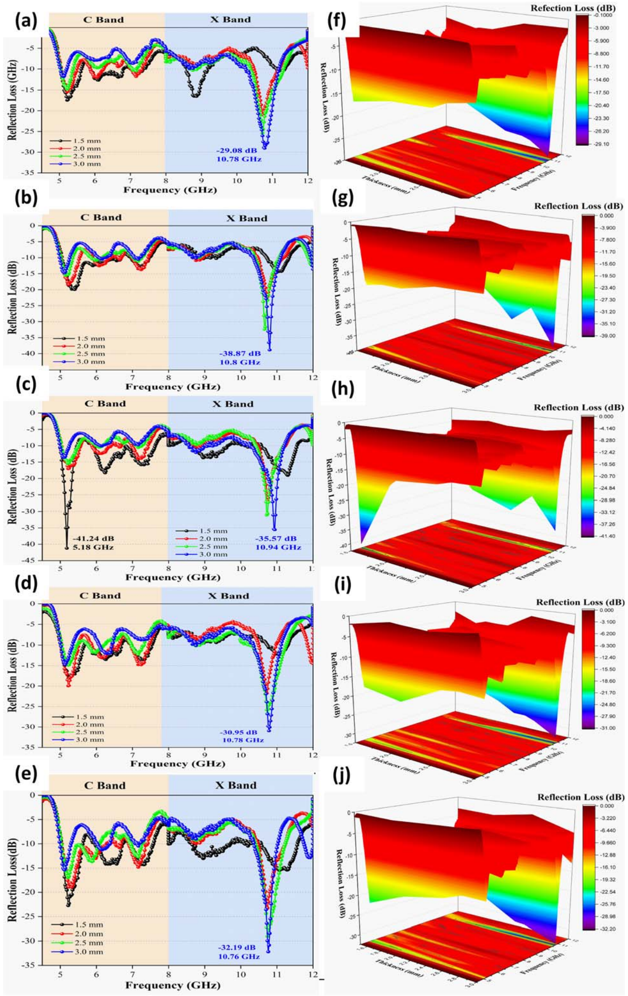

Fig. 9 RL of $BaFe_{12}O_{19}$@MnO_2 at 4–12 GHz frequency with different (a–c) hydrothermal temperatures (140–180) °C, (b–d–e) hydrothermal holding times (12–9–15) h, and (f–j) 3D representations.

Table 6 Summarizes current observations on ferrite matrix composites and their ability to reflect microwaves

Sample	Max RL (dB)	Frequency (GHz)	Thickness (mm)
$BaFe_{12}O_{19}$@MnO_2-170 (ref. 8)	−54.39	11.26	2.6
Fe_3O_4@MnO_2 (ref. 39)	−48.5	11.2	2.5
$NiFe_2O_4$@MnO_2@graphene[66]	−47.4	7.4	3
MoS_2@n-C@$CoFe_2O_4$ (ref. 67)	−46.7	12.5	2.4
Fe_3O_4/MnO_2 (ref. 38)	−43.6	9.2	3
$BaFe_{12}O_{19}$@$ZnFe_2O_4$/MWCNTs[32]	−42.3	8.2	2.5
Graphene@Fe_3O_4Nanocluster@C@MnO_2 (ref. 68)	−38.8	15	1.8
CF@$CoFe_2O_4$@MnO_2 (ref. 69)	−41	5.8	4
CF@$CoFe_2O_4$@MnO_2 (ref. 69)	−34	15.2	1.5
MnO_2@Fe-graphene[70]	−17.5	16	1.5
Ti_3SiC_2/$BaFe_{12}O_{19}$ (ref. 71)	−14.6	10.9	2.4
$BaFe_{12}O_{19}$@MnO_2-F (this study)	−41.24	5.18	1.5
$BaFe_{12}O_{19}$@MnO_2-D (this study)	−39.1	10.8	3

most effective hydrothermal temperature increase reduced reflection loss by 41.82%, from −29.08 dB to −41.24 dB. The lowest RL of −41.24 dB (5.18 GHz) was obtained at a hydrothermal temperature of 180 °C for the C band. This proves that an increase in hydrothermal temperature affects the nucleation rate of the core–shell composite $BaFe_{12}O_{19}$@MnO_2 and the growth of MnO_2 nanoflowers, agreeing with previous research works.[8] The increased hydrothermal holding time relatively reduces the reflection loss. The optimum hydrothermal holding time of 12 h shows a reflection loss of −38.87 dB in Fig. 9(b).

The chemical approach of coating the core with a shell can modify the core's characteristics, such as magnetism, electricity, wave absorption, and chemical stability.[65] The core–shell configuration produces a synergistic effect between the core and shell, optimizing the impedance characteristics and expanding the EM absorption bandwidth.[1,65] Based on the analysis of the greatest drop in RL at hydrothermal temperature change, the RL range was (−29.08 up to −41.24) dB, a difference of 12.16 dB. Following that, various $BaFe_{12}O_{19}:MnO_2$ mass ratios, which ranged from (−28.28 to −39.10) dB, demonstrated a difference of 10.82 dB. Finally, the variation in hydrothermal holding time resulted in an RL range of −30.95 to −38.87 dB, representing a 7.92 dB difference. Temperature (41.82%) and composition (38.26%) contributed more significantly to the decrease in RL than hydrothermal synthesis holding time (25.59%).

Table 6 shows information about the recently discovered microwave absorption characteristics of ferrite-containing composite materials. This shows that $BaFe_{12}O_{19}$@MnO_2 could be used as RAM. Several researchers proved that a core–shell composite is a hierarchical structure that can enhance the performance of RAMs. MnO_2 is widely preferred because of its dielectric properties and can be used as a booster for changing polarization and reducing RL. From Table 6, it can be seen that this study produced an RL of −41.24 dB (5.18 GHz, C band) and 99.99% absorption at the lowest sample thickness, *i.e.*, 1.5 mm. Additionally, the results of this study can also be applied to consider an antidetection aircraft coating with an absorption of 99.99% RL at −39.10 dB (10.8 GHz, X band) at 3 mm thickness. Radar wave absorption comprises two aspects: interference and radiation. Radar waves can be effectively absorbed by converting wave energy into heat or causing dissipation by means of interference. A remarkable RAM should possess high absorption power over a wide frequency range and low density.

The electrical permittivity and magnetic permeability of the absorber material distinguish them. Permittivity is a measure of a material's impact on an electromagnetic field, whereas permeability is a measure of the material's influence on a magnetic field. Eqn (3) and (4) indicate complex permittivity and complex permeability, respectively.[72]

$$\varepsilon_r = \varepsilon' - j\varepsilon'' \tag{3}$$

$$\mu_r = \mu' - j\mu'' \tag{4}$$

The electromagnetic characteristics are studied below in order to investigate the microwave absorption mechanism of $BaFe_{12}O_{19}$@MnO_2. In Fig. 10(a) and (b), both ε' and ε'' values show a similar trend across all of their frequency ranges. Increased MnO_2 composition in $BaFe_{12}O_{19}$ increases the permittivity of the $BaFe_{12}O_{19}$@MnO_2 core-cell composite, suggesting that MnO_2 can significantly increase the permittivity.[8,73] In general, real permittivity refers to energy storage, whereas imaginary permittivity denotes electric energy loss

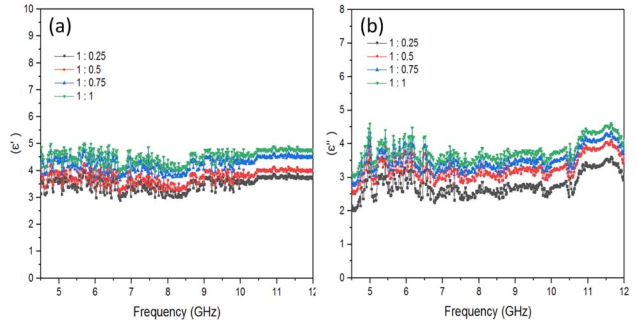

Fig. 10 Complex permittivity of $BaFe_{12}O_{19}$@MnO_2 (a) real parts (b) imaginary parts.

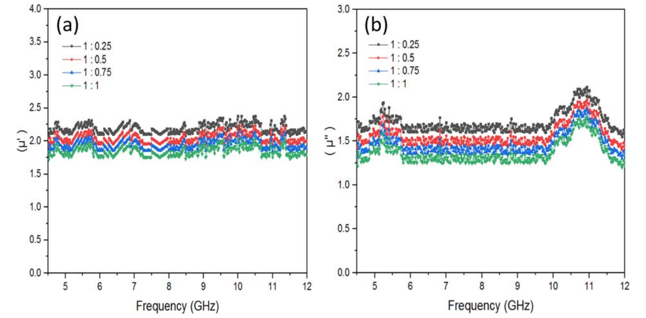

Fig. 11 Complex permeability of $BaFe_{12}O_{19}$@MnO_2 (a) real parts (b) imaginary parts.

capability.[74,75] The higher ratio composition of $BaFe_{12}O_{19}$@MnO_2 (1 : 1) can be attributed to the presence of interfacial polarization and enhanced dipolar polarization resulting from the numerous interfaces between MnO_2 and $BaFe_{12}O_{19}$, along with any residual defects.[66] Based on the principles of the free electron theory, the relationship between the imaginary part of the dielectric constant (ε'') and the electrical conductivity (σ) can be approximated as $\varepsilon'' \approx \sigma/2\pi\varepsilon_0 f$, where σ represents the electrical conductivity, ε_0 denotes the dielectric constant in vacuum, and f corresponds to the frequency.[76] The higher imaginary component of the $BaFe_{12}O_{19}$@MnO_2 (1 : 1) composites can be explained by their improved conductivity and excellent electronic transmission capability.

Fig. 11 demonstrates that an increase in the MnO_2 composition leads to a significant decrease in the complex permeability. The decline in permeability has an impact on the magnetic characteristics of coercivity (H_c), which decrease as the concentration of manganese dioxide increases, as confirmed in Table 4. Fig. 11(a) and (b) illustrate the relative complex permeability. The value of μ' experiences fluctuations within the range of 1.75–2.25 and demonstrates a peak in frequency between 10 and 12 GHz due to natural ferromagnetic resonance and exchange resonance.[77] Additionally, it remains rather constant throughout the 6–10 GHz frequency.

Fig. 12(a) illustrates the dielectric loss tangent ($\tan\delta\varepsilon = \varepsilon''/\varepsilon'$) that corresponds to the given data. The largest dielectric loss occurs at a composition ratio of 1 : 0.5, indicating that the $BaFe_{12}O_{19}$@MnO_2 composites possess enhanced dielectric loss capacity. The magnetic loss tangent, represented as $\tan\delta\mu = \mu''/\mu'$, is illustrated in Fig. 12(b). In Fig. 12(b), the greatest magnetic loss tangent occurs at a ratio of 1 : 1. The condition is very relevant, with the highest absorption at the composition ratio of $BaFe_{12}O_{19}$: MnO_2 at 1 : 1, as shown in Fig. 8(d). The absorption of larger electromagnetic waves is influenced by the magnetic loss that affects its magnetic properties.

Moreover, it can be observed that the tan $\delta\mu$ are smaller than the tan $\delta\varepsilon$, indicating that the primary factor contributing to loss in these materials is the dielectric structure.

Fig. 13 show schematic illustration of microwave absorption mechanisms of $BaFe_{12}O_{19}$@MnO_2 core–shell composites. In general, the microwave absorption mechanism of $BaFe_{12}O_{19}$@MnO_2 core–shell composites is quite complex and involves multiple processes. The microwave signal is attenuated by the magnetic and dielectric losses exhibited by the composite material. Due to the presence of $BaFe_{12}O_{19}$, which has high magnetic permeability and generates Eddy currents in response to an applied electromagnetic field, magnetic loss occurs.[78] Furthermore, $BaFe_{12}O_{19}$ has large magneto-crystalline anisotropy, which leads to high reflection loss.[79] Besides that, due to the presence of MnO_2 nanoflowers, which have a high dielectric constant and can store energy in an electric field, the dielectric loss occurs.[80] Dielectric loss is observed when an electromagnetic wave traverses a substance, inducing the polarization of its constituent molecules. The phenomenon of polarization gives rise to thermal effects, leading to the dissipation of energy and the reduction in the intensity of the electromagnetic wave.[34,35] The delay of dipoles in turn around with an external electromagnetic field would consume the incident microwave.[78]

The mechanisms present in the composite material include assistant Eddy current, magnetic resonance loss, as well as enhanced impedance matching, magneto crystalline anisotropy, dielectric loss, and also other mechanisms like primary nature and exchange resonance, destructive interference, multiple reflection and scattering effect, and the subordinate effect of dipole and interface polarization loss[81] all contribute to further reduce the microwave signal and improve the material's absorption performance. Furthermore, measuring the complex permittivity ($\varepsilon_r = \varepsilon' - j\varepsilon''$) and complex permeability ($\mu_r = \mu' - j\mu''$) of the material determines the electromagnetic response of the

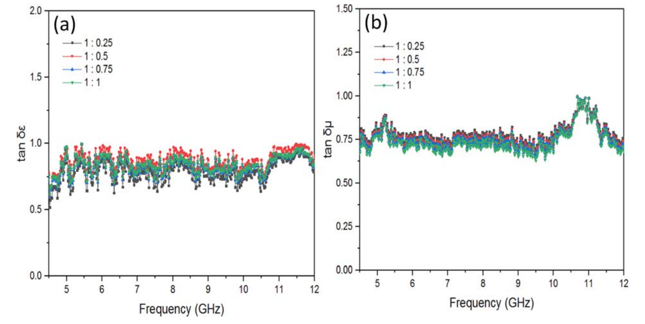

Fig. 12 (a) Dielectric loss tangent (b) magnetic loss tangent of $BaFe_{12}O_{19}$@MnO_2.

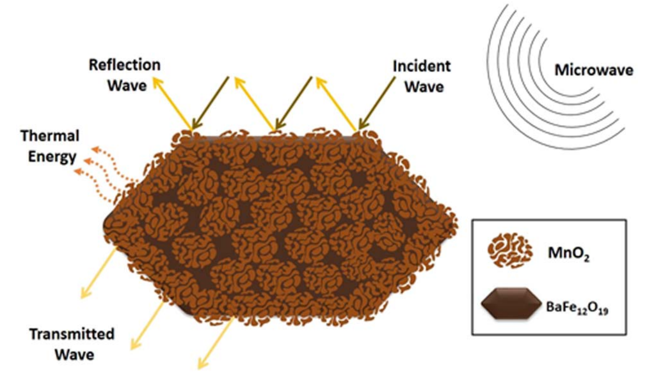

Fig. 13 Schematic illustration of microwave absorption mechanisms of $BaFe_{12}O_{19}$@MnO_2 core–shell composites.

composite absorber.[82] The real parts of these parameters represent storage capacity for electromagnetic waves, whereas the imaginary parts represent dissipation capacity. The maximum amount of EM radiation can be absorbed by an absorber when its input impedance is close to the impedance of a free space.[33] The present study focuses on the optimization of $BaFe_{12}O_{19}$@MnO_2 core–shell composites with the aim of enhancing their dielectric loss properties. This is achieved through the precise control of the morphology and distribution of MnO_2 nanoflower on the $BaFe_{12}O_{19}$ surface. This is due to the proper morphology, precursor ratio composition, temperature, and hydrothermal holding time. Overall, the $BaFe_{12}O_{19}$@MnO_2 exhibits a synergistic impact of several absorption mechanisms that work in concert to give strong and broad electromagnetic absorption in the C and X band frequencies.

Conclusions

The single-phase core–shell $BaFe_{12}O_{19}$@MnO_2 composite was successfully synthesized using molten salt and hydrothermal methods. The particle size of $BaFe_{12}O_{19}$@MnO_2 increased by 288% with an increase in temperature and hydrothermal holding time, but only by 213% with an increase in the MnO_2 mass fraction. The hydrothermal temperature is identified as the most influential synthesis parameter, resulting in a significant reduction in reflection loss of up to 41.82%. Additionally, the composition mass ratio of $BaFe_{12}O_{19}:MnO_2$ exhibits a decrease of 38.26%, while the hydrothermal holding time demonstrates a comparatively smaller reduction of 25.59%. The study observed that the density, quantity, and thickness of the MnO_2 sheets exhibited a tendency toward increase as the temperature and hydrothermal holding time increased. The composite material $BaFe_{12}O_{19}$@MnO_2 showed a notable reduction in reflection loss, reaching a value of −41.24 dB at a frequency of 5.18 GHz, resulting in 99.99% absorption. This achievement was obtained by optimizing the synthesis parameters, specifically by utilizing a $BaFe_{12}O_{19}:MnO_2$ mass ratio of 1 : 0.5 and a thickness of 1.5 mm. The synthesis process was conducted at a temperature of 180 °C with a holding time of 12 h.

Author contributions

Erlina Yustanti: conceptualization, methodology, supervision, funding acquisition, writing – reviewing and editing, project administration. Alfian Noviyanto: formal analysis, visualization, resources, supervision. Muhammad Ikramullah: data curation, formal analysis, investigation. Yogie Anes Marsillam: formal analysis, investigation, writing – original draft. Yana Taryana: software, validation, Ahmad Taufiq: formal analysis, data curation.

Conflicts of interest

There are no conficts to declare.

Acknowledgements

The Ministry of Education, Culture, Research, and Technology of the Republic of Indonesia provided the PDKN research grant with contract number B/389/UN43.9/PT.00.03/2023 that fully funded this project.

References

1 L. Gai, H. Zhao, F. Wang, P. Wang, Y. Liu, X. Han and Y. Du, *Nano Res.*, 2022, **15**, 9410–9439.
2 X. Meng, L. He, Y. Liu, Y. Yu and W. Yang, *Carbon N. Y.*, 2022, **194**, 207–219.
3 H. Pang, Y. Duan, L. Huang, L. Song, J. Liu, T. Zhang, X. Yang, J. Liu, X. Ma, J. Di and X. Liu, *Composites, Part B*, 2021, **224**, 109173.
4 L. Wang, B. Wen, X. Bai, C. Liu and H. Yang, *J. Colloid Interface Sci.*, 2019, **540**, 30–38.
5 P. Xu, J. Fang, H. He and X. Yue, *J. Alloys Compd.*, 2022, **903**, 163826.
6 B. Dai, Y. Ma, F. Dong, J. Yu, M. Ma, H. K. Thabet, S. M. El-Bahy, M. M. Ibrahim, M. Huang, I. Seok, G. Roymahapatra, N. Naik, B. Bin Xu, J. Ding and T. Li, *Adv. Compos. Hybrid Mater.*, 2022, **5**, 704–754.
7 J. Cheng, H. Zhang, Y. Xiong, L. Gao, B. Wen, H. Raza, H. Wang, G. Zheng, D. Zhang and H. Zhang, *J. Mater.*, 2021, **7**, 1233–1263.
8 F. Hu, H. Nan, M. Wang, Y. Lin, H. Yang, Y. Qiu and B. Wen, *Ceram. Int.*, 2021, **47**, 16579–16587.
9 V. P. Singh, R. Jasrotia, R. Kumar, P. Raizada, S. Thakur, K. M. Batoo and M. Singh, *World J. Condens. Matter Phys.*, 2018, **8**, 36–61.
10 G. Gultom, M. Rianna, P. Sebayang and M. Ginting, *Case Stud. Therm. Eng.*, 2020, **18**, 100580.
11 G. Asghar, S. Asri, S. N. Khusro, G. H. Tariq, M. S. Awan, M. Irshad, A. Safeen, Y. Iqbal, W. H. Shah and M. Anis-ur-Rehman, *J. Electron. Mater.*, 2020, **49**, 4318–4323.
12 M. K. Manglam, S. Kumari, J. Mallick and M. Kar, *Appl. Phys. A: Mater. Sci. Process.*, 2021, **138**, 1–12.
13 Z. Liu, Y. Cui, Q. Li, Q. Zhang and B. Zhang, *J. Colloid Interface Sci.*, 2022, **607**, 633–644.
14 J. Liao, J. Qiu, G. Wang, R. Du, N. Tsidaeva and W. Wang, *J. Colloid Interface Sci.*, 2021, **604**, 537–549.
15 C. Cui, R. Guo, E. Ren, H. Xiao, M. Zhou, X. Lai, Q. Qin, S. Jiang and W. Qin, *Chem. Eng. J.*, 2021, **405**, 126626.
16 M. Qiao, X. Lei, Y. Ma, L. Tian, W. Wang, K. Su and Q. Zhang, *J. Alloys Compd.*, 2017, **693**, 432–439.
17 B. Quan, X. Liang, G. Ji, Y. Cheng, W. Liu, J. Ma, Y. Zhang, D. Li and G. Xu, *J. Alloys Compd.*, 2017, **728**, 1065–1075.
18 J. Gao, Q. Ding, P. Yan, Y. Liu, J. Huang, T. Mustafa, R. Guo, X. Lu, K. Wang, S. Sun, X. Feng, W. Luo, Y. Fan and W. Jiang, *J. Eur. Ceram. Soc.*, 2022, **42**, 993–1000.
19 J. Ma, W. Li, Y. Fan, J. Yang, Q. Yang, J. Wang, W. Luo, W. Zhou, N. Nomura, L. Wang and W. Jiang, *ACS Appl. Mater. Interfaces*, 2019, **11**, 46386–46396.

20 W. Luo, M. Wang, K. Wang, P. Yan, J. Huang, J. Gao, T. Zhao, Q. Ding, P. Qiu, H. Wang, P. Lu, Y. Fan and W. Jiang, *Adv. Sci.*, 2022, **9**, 2104163.

21 R. Yang, Y. Fan, R. Ye, Y. Tang, X. Cao, Z. Yin and Z. Zeng, *Adv. Mater.*, 2021, **33**, 1–53.

22 E. Yustanti, A. Trenggono and A. Manaf, *Int. J. Technol.*, 2020, **11**, 310–321.

23 E. Yustanti, V. Hafidzatul Hakimah, A. Noviyanto, M. Randa and M. Manawan, *Mater. Today Proc.*, 2023, **80**, 704–709.

24 E. Yustanti, A. Noviyanto, L. C. Chotimah, M. A. R. Saputra, M. Randa and M. Manawan, *Coatings*, 2022, **12**, 1367.

25 M. Rianna, M. Situmorang, C. Kurniawan, A. P. Tetuko, E. A. Setiadi, M. Ginting and P. Sebayang, *Mater. Lett.*, 2019, **256**, 126612.

26 M. Rianna, T. Sembiring, M. Situmorang, C. Kurniawan, A. P. Tetuko, E. A. Setiadi, I. Priyadi, M. Ginting and P. Sebayang, *Case Stud. Therm. Eng.*, 2019, **13**, 100393.

27 Q. Liang, Z. Tong, J. Guo, M. Wang, Q. Yao and H. Zhou, *J. Magn. Magn. Mater.*, 2021, **539**, 168400.

28 S. Goel, A. Garg, H. B. Baskey and S. Tyagi, *J. Sol-Gel Sci. Technol.*, 2021, **98**, 351–363.

29 Z. Qu, Y. Wang, P. Yang, W. Zheng, N. Li, J. Bai, Y. Zhang, K. Li, D. Wang, Z. Liu, K. Yao, R. Li and Y. Zhang, *Molecules*, 2022, **27**, 1–14.

30 Y. Lin, Y. Liu, J. Dai, L. Wang and H. Yang, *J. Alloys Compd.*, 2018, **739**, 202–210.

31 Y. Liu, Y. Lin and H. Yang, *J. Alloys Compd.*, 2019, **805**, 130–137.

32 M. Lu, J. Wang, X. Su, Q. Wu, T. Yan and X. Zhang, *Mater. Lett.*, 2019, **253**, 46–49.

33 M. Chang, Z. Jia, G. Wu and P. Yin, *Appl. Phys. Lett.*, 2023, **122**, 131901.

34 T. Hou, J. Wang, T. Zheng, Y. Liu, G. Wu and P. Yin, *Small*, 2023, 2303463.

35 T. Zheng, Y. Zhang, Z. Jia, J. Zhu, G. Wu and P. Yin, *Chem. Eng. J.*, 2023, **457**, 140876.

36 M. A. Almessiere, Y. Slimani, A. D. Korkmaz, A. Baykal, H. Güngüneş, H. Sözeri, S. E. Shirsath, S. Güner, S. Akhtar and A. Manikandan, *RSC Adv.*, 2019, **9**, 30671–30684.

37 H. Yang, X. Zhang, Z. Xiong, Z. Shen, C. Liu and Y. Xie, *Ceram. Int.*, 2021, **47**, 2155–2164.

38 X. Liu, N. Wu, C. Cui, N. Bi and Y. Sun, *RSC Adv.*, 2015, **5**, 24016–24022.

39 M. Qiao, X. Lei, Y. Ma, L. Tian, K. Su and Q. Zhang, *Chem. Eng. J.*, 2016, **304**, 552–562.

40 M. Wang, Y. Lin, H. Yang, Y. Qiu and S. Wang, *J. Alloys Compd.*, 2020, **817**, 153265.

41 A. Manaf, M. A. E. Hafizah, B. Belyamin, B. Nainggolan and M. T. E. Manawan, *Int. J. Technol.*, 2017, **3**, 458–465.

42 Y. Li, J. Wang, Y. Zhang, M. N. Banis, J. Liu, D. Geng, R. Li and X. Sun, *J. Colloid Interface Sci.*, 2012, **369**, 123–128.

43 F. Gan, Q. Yao, L. Cheng, L. Zhang, Q. Liang, J. Guo, M. Wang, H. Zhou and Y. Zhong, *J. Alloys Compd.*, 2022, **897**, 162964.

44 X. Hao, J. Zhao, Y. Song and Z. Huang, *J. Nano Res.*, 2018, **53**, 1–6.

45 D. B. Hovis and K. T. Faber, *Scr. Mater.*, 2001, **44**, 2525–2529.

46 H. Li, H. Wang, M. Yang, Y. Sun, Y. Yin and P. Guo, *Colloids Surf., A*, 2020, **602**, 125068.

47 K. Bai, J. Hao, Y. Yang and A. Qian, *Heliyon*, 2020, **6**, e04436.

48 A. A. Egorova, T. M. Bushkova, I. V. Kolesnik, A. D. Yapryntsev, S. Y. Kottsov and A. E. Baranchikov, *Russ. J. Inorg. Chem.*, 2021, **66**, 146–152.

49 A. M. Toufiq, F. Wang, Q. U. A. Javed and Y. Li, *Mod. Phys. Lett. B*, 2014, **28**, 1–8.

50 J. Edianta, N. Fauzi, M. Naibaho, F. S. Arsyad and I. Royani, *Sci. Technol. Indones.*, 2021, **6**, 39–52.

51 M. K. Rasmussen, J. N. Pedersen and R. Marie, *Nat. Commun.*, 2020, **11**, 1–8.

52 A. Bahadur, A. Saeed, S. Iqbal, M. Shoaib, I. Ahmad, M. S. ur Rahman, M. I. Bashir, M. Yaseen and W. Hussain, *Ceram. Int.*, 2017, **43**, 7346–7350.

53 S. D. Johnson, D. S. Park, S. B. Qadri and E. P. Gorzkowski, *J. Magn. Magn. Mater.*, 2019, **479**, 156–160.

54 S. Ranjit, K. M. Law, S. Budhathoki, J. M. Allred, R. A. Rosenberg, D. S. Park, S. Johnson and A. J. Hauser, *J. Am. Ceram. Soc.*, 2020, **103**, 1542–1548.

55 R. Sato and R. Grossinger, *Indones. J. Mater. Sci.*, 2003, **5**, 13–17.

56 S. Tumanski, *Handbook of Magnetic Measurements*, CRC Press, Boca Raton, 1st edn, 2011.

57 K. Ali, A. Bahadur, A. Jabbar, S. Iqbal, I. Ahmad and M. I. Bashir, *J. Magn. Magn. Mater.*, 2017, **434**, 30–36.

58 H. R. Luthfianti, W. Widanarto, S. K. Ghoshal, M. Effendi and W. T. Cahyanto, *J. Phys.: Conf. Ser.*, 2020, **1494**, 012043.

59 A. K. Sahu, R. Aravind and G. S. Brahma, *Mater. Today: Proc.*, 2021, **49**, 1762–1768.

60 N. Adeela, U. Khan, M. Iqbal, S. Riaz, H. Ali, K. Maaz and S. Naseem, *J. Electron. Mater.*, 2016, **45**, 5853–5859.

61 A. Susilawati, Doyan and Khalilurrahman, in *AIP Conference Proceedings*, AIP Publishing, America, 2017, vol. 1801, p. 040007.

62 Y. Shao, W. Lu, H. Chen, J. Q. Xiao, Y. Qiu and T. Chou, *Composites Part B*, 2018, **144**, 111–117.

63 Z. Zhang, S. Wang, Y. Lv, X. Chen, Z. Wu and Y. Zou, *J. Alloys Compd.*, 2019, **810**, 151744.

64 E. Handoko, I. Sugihartono, S. Budi, M. Randa, Z. Jalil and M. Alaydrus, *J. Phys.: Conf. Ser.*, 2018, **1080**, 012002.

65 W. Shao, M. Liu, G. Tong, T. Wu and T. Lv, *J. Mater. Sci.*, 2021, **56**, 10293–10311.

66 Y. Wang, Y. Fu, X. Wu, W. Zhang, Q. Wang and J. Li, *Ceram. Int.*, 2017, **43**, 11367–11375.

67 X. Chen, W. Wang, T. Shi, G. Wu and Y. Lu, *Carbon N. Y.*, 2020, **163**, 202–212.

68 L. Wang, Y. Huang, C. Li, J. Chen and X. Sun, *Phys. Chem. Chem. Phys.*, 2015, **17**, 5878–5886.

69 A. Feng, T. Hou, Z. Jia and G. Wu, *R. Soc. Chem. Adv.*, 2020, **10**, 10510–10518.

70 H. Lv, G. Ji, X. Liang, H. Zhang and Y. Du, *J. Mater. Chem. C*, 2015, **3**, 5056–5064.

71 Y. Liu, X. Su, F. Luo, J. Xu, J. Wang, X. He and Y. Qu, *J. Electron. Mater.*, 2019, **48**, 2364–2372.

72 X. Zeng, C. Zhao, Y. Yin, T. Nie, N. Xie, R. Yu and G. D. Stucky, *Carbon N. Y.*, 2022, **193**, 26–34.

73 Z. Gao, Z. Jia, K. Wang, X. Liu, L. Bi and G. Wu, *Chem. Eng. J.*, 2020, **402**, 125951.
74 H. Sun, R. Che, X. You, Y. Jiang, Z. Yang, J. Deng, L. Qiu and H. Peng, *Adv. Mater.*, 2014, **26**, 8120–8125.
75 K. Wang, Y. Chen, R. Tian, H. Li, Y. Zhou, H. Duan and H. Liu, *ACS Appl. Mater. Interfaces*, 2018, **10**, 11333–11342.
76 B. Quan, W. Gu, J. Sheng, X. Lv, Y. Mao, L. Liu, X. Huang, Z. Tian and G. Ji, *Nano Res.*, 2021, **14**, 1495–1501.
77 Y. Cheng, J. Z. Y. Seow, H. Zhao, Z. J. Xu and G. Ji, *Nano-Micro Lett.*, 2020, **12**, 1–15.
78 P. Yin, G. Wu, Y. Tang, S. Liu, Y. Zhang, G. Bu, J. Dai, Y. Zhao and Y. Liu, *Chem. Eng. J.*, 2022, **446**, 136975.
79 M. Z. Khan, I. H. Gul, F. Javaid, A. Ali, S. Hafeez and M. M. Baig, *Mater. Res. Bull.*, 2023, **168**, 112468.
80 A. C. Sparavigna, *SSRN Electron. J.*, 2023, 1–27.
81 Y. Luo, P. Yin, G. Wu, L. Zhang, G. Ma, J. Wang, X. Sun and G. Bu, *Carbon N. Y.*, 2022, **197**, 389–399.
82 T. Cheng, Y. Guo, Y. Xie, L. Zhao, T. Wang, A. Meng, Z. Li and M. Zhang, *Carbon N. Y.*, 2023, **206**, 181–191.